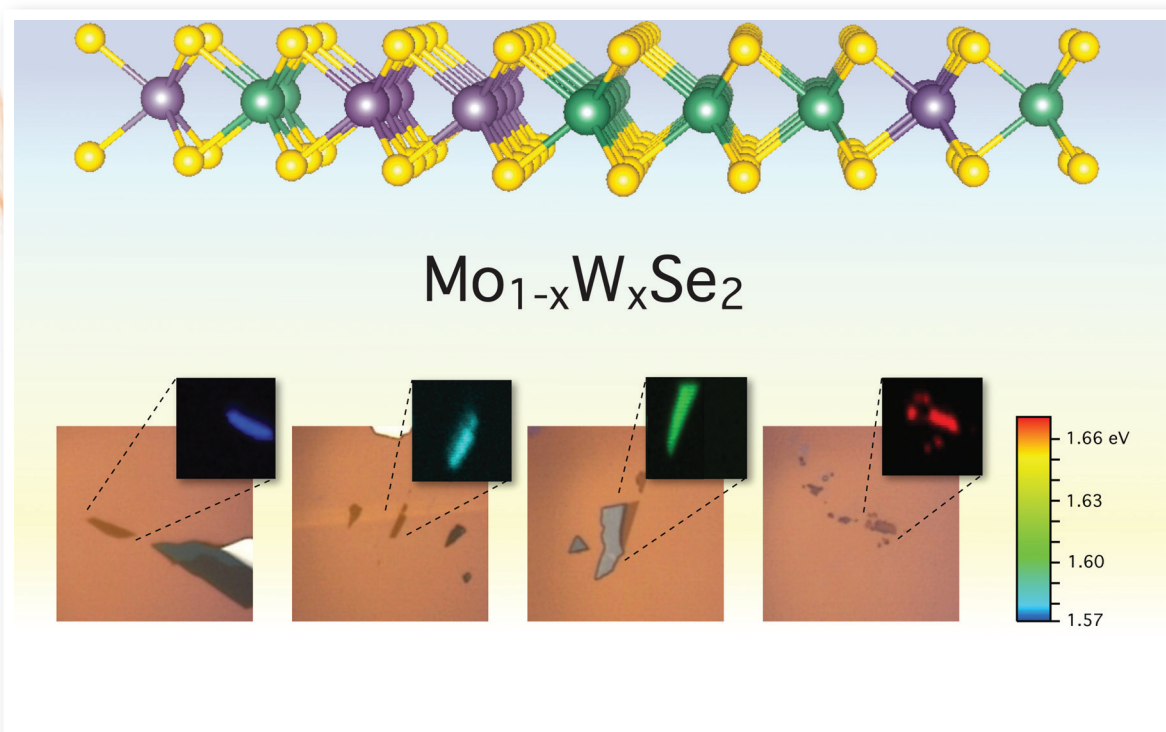


AIP | Applied Physics Letters



Two-dimensional semiconductor alloys: Monolayer $\text{Mo}_{1-x}\text{W}_x\text{Se}_2$

Sefaattin Tongay,^{1,2,a)} Deepa S. Narang,³ Jun Kang,^{2,4} Wen Fan,¹ Changhyun Ko,¹ Alexander V. Luce,^{1,4} Kevin X. Wang,¹ Joonki Suh,^{1,2} K. D. Patel,⁵ V. M. Pathak,⁵ Jingbo Li,² and Junqiao Wu^{1,2,4}

¹Department of Materials Science and Engineering, University of California, Berkeley, California 94720, USA

²State Key Laboratory of Superlattices and Microstructures, Institute of Semiconductors,

Chinese Academy of Sciences, P.O. Box 912, Beijing 100083, People's Republic of China

³Department of Physics, Alliance College of Engineering and Design (ACED), Alliance University, Chandapura, Anekal, Bangalore 562106, Karnataka, India

⁴Materials Sciences Division, Lawrence Berkeley National Laboratory, Berkeley, California 94720, USA

⁵Department of Physics, Sardar Patel University, Vallabh Vidyanagar – 388120, Anand, Gujarat, India

(Received 22 September 2013; accepted 13 November 2013; published online 2 January 2014)

Monolayer $\text{Mo}_{1-x}\text{W}_x\text{Se}_2$ ($x=0, 0.14, 0.75$, and 1) alloys were experimentally realized from synthesized crystals. $\text{Mo}_{1-x}\text{W}_x\text{Se}_2$ monolayers are direct bandgap semiconductors displaying high luminescence and are stable in ambient. The bandgap values can be tuned by varying the W composition. Interestingly, the bandgap values do not scale linearly with composition. Such non-linearity is attributed to localization of conduction band minimum states around Mo d orbitals, whereas the valence band maximum states are uniformly distributed among W and Mo d orbitals. Results introduce monolayer $\text{Mo}_{1-x}\text{W}_x\text{Se}_2$ alloys with different gap values, and open a venue for broadening the materials library and applications of two-dimensional semiconductors.

© 2014 AIP Publishing LLC. [<http://dx.doi.org/10.1063/1.4834358>]

Layered semiconductors at the quantum limit are emerging as an important class of materials for optoelectronics and microelectronics technologies.^{1–5} Unlike the enormous number of existing bulk semiconductors, the full potential of these two-dimensional (2D) semiconductors is severely limited by the small number of members currently available. To remove these limits, their optical properties have been tuned by thermal annealing,^{6,7} molecular adsorption,⁷ defect engineering,^{8,9} and application of external strain.¹⁰ Similarly, alloying in materials provides a versatile, stable, and industrially scalable way to tune the physical properties to optimize and widen their potential application venues.^{11–13} Previously, alloys of transition metal dichalcogenides have been theoretically demonstrated¹¹ and $\text{Mo}_{1-x}\text{W}_x\text{S}_2$ crystals have been experimentally realized to vary their bandgap values.¹³

Here, we demonstrate transition metal dichalcogenide (TMD) monolayer alloys $\text{Mo}_{1-x}\text{W}_x\text{Se}_2$. The monolayers were isolated from $\text{Mo}_{1-x}\text{W}_x\text{Se}_2$ crystals with different tungsten (W) composition ($x=0, 0.14, 0.75$, and 1) by conventional mechanical exfoliation technique. These $\text{Mo}_{1-x}\text{W}_x\text{Se}_2$ monolayers are fully alloyed, i.e., phase separation is absent as determined by nano Auger electron spectroscopy (nano-AES) and also density functional theory calculations. These monolayers are stable in ambient and are direct-bandgap semiconductors with high photoluminescence (PL) efficiency. By varying the W composition, the fundamental bandgap values are tuned from 1.56 eV ($x=0$) to 1.67 eV ($x=1$). Interestingly, the bandgap composition dependence deviates from a linear interpolation with relatively large band bowing parameter ($0.14\text{ eV} > E_g(\text{WSe}_2) - E_g(\text{MoSe}_2) = 0.11\text{ eV}$). These results are analyzed and interpreted using density functional theory (DFT) calculations.

The bulk crystals were grown by direct vapor transport technique (Fig. 1(a)). Custom-made quartz ampoules (24 cm in length and 2.5 cm in diameter) were thoroughly cleaned and the ampoule was etched for 12 h using concentrated HF at 80°C to roughen the inside wall of the tube to facilitate the crystal growth. Mo, W, and Se powders (-325 mesh, purity 99.995% metal basis) were mixed in stoichiometric proportions and placed in the ampoule. The ampoules were pumped down to the lowest attainable pressures in our system (10^{-5} Torr), and sealed immediately to avoid blasting due to high vapor pressure developed inside the ampoule at growth temperatures. The ampoules were inserted into a two-zone tube furnace system, and the system was heated up to 1080°C with 50°C/h rate. Samples were left at constant temperature for 3 days. During the growth phase, the temperature of the growth zone (T_g) was gradually lowered down to 1000°C at the rate of 2°C/h and the source temperature (T_s) was maintained at 1080°C . After 4 days, the system was cooled down to room temperature at a 50°C/h rate. The growth typically yielded shiny, large, layered, and easy-to-exfoliate crystals that are 2–10 mm in size with high crystallinity. The crystals were characterized using scanning electron microscopy (SEM), PL, Raman, Rutherford backscattering spectrometry (RBS), x-ray photoelectron (XPS), and nano-AES techniques.

The alloy compositions were determined by RBS with a 3.04 MeV He^{2+} beam. Backscattered He ions were detected by a Si surface barrier detector at 168° backscattering angle. RBS measurements yield $x=0, 0.14, 0.75$, and 1 with 0.01 and higher accuracy. XPS spectra taken from the $\text{Mo}_{1-x}\text{W}_x\text{Se}_2$ crystals also confirmed the presence of Mo, W, and Se (Fig. 1(b)). The MoSe_2 ($x=0$) crystals displayed Mo $3d_{5/2}$ and $3d_{3/2}$ photoelectron lines at 229 and 231 eV, respectively. As the W composition increased, the intensity of these two peaks gradually decreased and the W $4d_{5/2}$ and

^{a)}Electronic mail: tongay@berkeley.edu

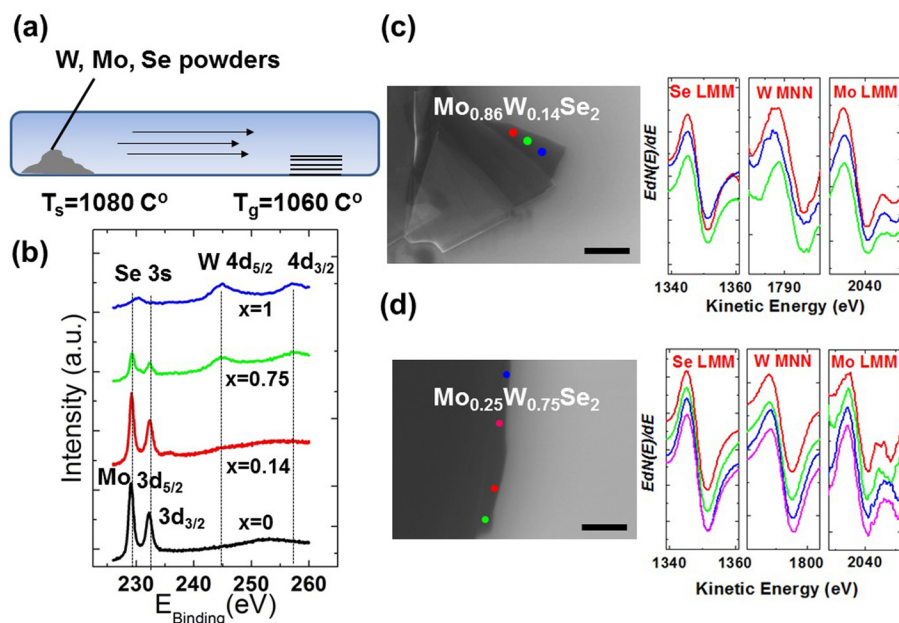


FIG. 1. (a) Schematics of the direct vapor transport method for the $\text{Mo}_{1-x}\text{W}_x\text{Se}_2$ crystal growth. (b) XPS data taken on the $\text{Mo}_{1-x}\text{W}_x\text{Se}_2$ bulk crystals for $x = 0, 0.14, 0.75$, and 1. (c)–(d) Typical SEM images (scale bar is 1 μm) taken from exfoliated monolayer and nano-AES spectra for Se, W, and Mo, showing that the monolayers are not phase separated.

$4d_{3/2}$ peaks developed at 245 and 257 eV. At $x = 1$ (WSe_2), Mo $3d_{5/2}$ and $3d_{3/2}$ peaks completely disappeared and the weak Se 3s peak became visible at 230 eV. Since the XPS spot size is larger than $5\text{ mm} \times 5\text{ mm}$, it does not provide any information if the synthesized crystals are phase separated in nature. To eliminate the possibility of phase separation, especially that inside each layer, we have performed nano-AES measurement with 10 nm spatial resolution on multiple spots across exfoliated monolayers. These monolayer $\text{Mo}_{1-x}\text{W}_x\text{Se}_2$ flakes were mechanically exfoliated from the bulk crystals onto 90 nm SiO_2/Si substrates and the thickness of the SiO_2 was chosen to maximize the optical contrast of the flakes. The thickness of the monolayers was 0.7 nm, as determined by atomic force microscopy (AFM) line scan. In Figs. 1(c) and 1(d), we show the SEM images and nano-AES data taken from $\text{Mo}_{0.86}\text{W}_{0.14}\text{Se}_2$ and $\text{Mo}_{0.25}\text{W}_{0.75}\text{Se}_2$ monolayers. Dots on the monolayers illustrate where the nano-AES measurement was performed, and color of the dot correspond to individual solid line in the AES spectra. Nano-AES measurements show that the elemental composition does not vary spatially but remain at $x = 0.14$ and $x = 0.75$, respectively, and therefore, we eliminate the possibility of phase separation in monolayers. Complete miscibility of the alloy is also confirmed by our DFT calculations and will be discussed later.

The monolayers were stable in ambient conditions, and showed no sign of deterioration for more than 3 months. The micro-PL data were taken on $\text{Mo}_{1-x}\text{W}_x\text{Se}_2$ monolayers using 488 nm laser (10 μW) on a $\sim 7\text{ }\mu\text{m}^2$ area. PL mapping on the monolayer $\text{Mo}_{1-x}\text{W}_x\text{Se}_2$ shows that the monolayers

are highly luminescent and the integrated PL intensity is spatially uniform (Figs. 2(a)–2(d)). As shown in Figs. 2(a)–2(d), the PL peak position of the monolayers can be tuned between 1.56 eV for MoSe_2 ($x = 0$) and 1.67 eV for WSe_2 ($x = 1$). Next, we compare the integrated PL intensity of $\text{Mo}_{1-x}\text{W}_x\text{Se}_2$ monolayers to other semiconducting TMDs, such as MoS_2 , MoSe_2 , WS_2 , and WSe_2 , by measuring the integrated PL intensity at the same laser excitation power, spot size, laser wavelength, and exposure time. We find that the $\text{Mo}_{1-x}\text{W}_x\text{Se}_2$ monolayers are two orders of magnitude more luminescent than monolayer MoS_2 , and one order of magnitude more than that of monolayer MoSe_2 whereas it is as luminescent as WSe_2 and WS_2 monolayers. Strong luminescence in the monolayer implies that the $\text{Mo}_{1-x}\text{W}_x\text{Se}_2$ monolayers are also direct gap semiconductors similar to other semiconducting TMDs and differences in the integrated PL intensities might be related to intrinsic material parameters such as radiative and non-radiative recombination times as well as the differences in the material quality/crystallinity.

The MoSe_2 monolayers display a prominent Raman mode, the out-of-plane A_g mode, at 241 cm^{-1} , whereas the WSe_2 monolayers show two peaks at 251 and 261 cm^{-1} , consistent with previously reported values.^{6,14,15} The Raman spectrum of the monolayer $\text{Mo}_{1-x}\text{W}_x\text{Se}_2$ show a peak around 244.5 and 249.2 cm^{-1} for $x = 0.14$ and 0.75, respectively. Overall, the Raman peak positions scale linearly with the W composition as shown in Fig. 3(c).

The PL measurements on the monolayer $\text{Mo}_{1-x}\text{W}_x\text{Se}_2$ reveal that the PL peak position and hence the bandgap

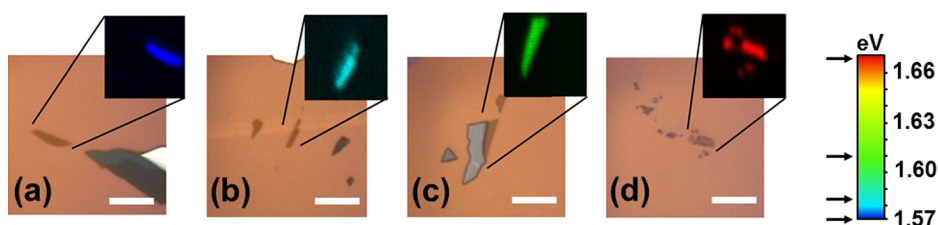


FIG. 2. Optical images and PL mapping data taken on monolayers of (a) MoSe_2 ($x = 0$), (b) $\text{Mo}_{0.86}\text{W}_{0.14}\text{Se}_2$ ($x = 0.14$), (c) $\text{Mo}_{0.25}\text{W}_{0.75}\text{Se}_2$ ($x = 0.75$), and (d) WSe_2 ($x = 1$). Scale bar is 5 μm .

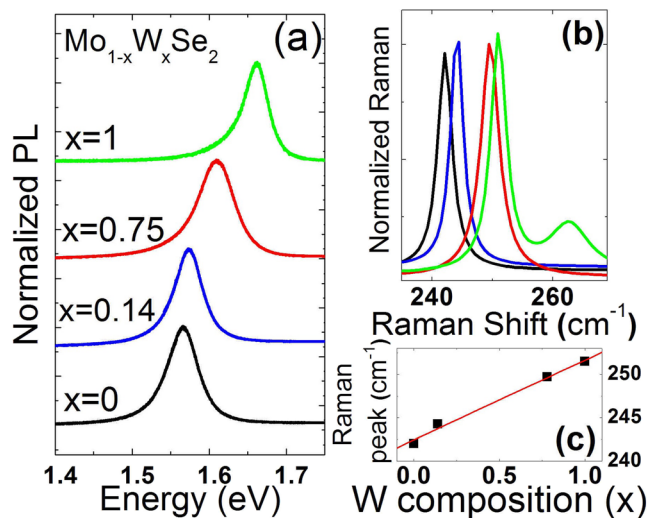


FIG. 3. (a) Micro-PL and (b) micro-Raman (A_{1g}) spectra taken on the monolayer MoSe_2 (black), $\text{Mo}_{0.86}\text{W}_{0.14}\text{Se}_2$ (blue), $\text{Mo}_{0.25}\text{W}_{0.75}\text{Se}_2$ (red), and WSe_2 (green). (c) Raman peak position with respect to the W composition (x). The solid red line is a linear fitting.

values can be tuned by varying the W composition. Unlike the Raman spectrum, the bandgap values do not scale linearly with the composition, instead display band bowing effect as shown in Fig. 4(a). Fitting to the conventional bowing equation, $E_g(x) = xE_g(1) + (1-x)E_g(0) - bx(1-x)$, with bandgap bowing parameter, b , as the only adjustable parameter yields $b = 0.14$ eV, which is higher than the difference between the bandgap values of WSe_2 and MoSe_2 , 0.11 eV. Previously, giant bandgap bowing effect has been observed in conventional semiconductor alloys with large structural/chemical mismatch, and the large bowing coefficient has been mostly attributed to the valence band maximum (VBM) or conduction band minimum (CBM) wavefunctions strongly localized at one of the constituents in the crystal alloy.¹⁶ Within this perspective, our results are rather surprising as the MoSe_2 and WSe_2 are isostructural, Mo and W differ by less than 10% in terms of atomic size and electronegativity, and Mo and W show only moderate chemical differences.^{17,18}

Consistent with our experimental findings, the calculated electronic band structures of $\text{Mo}_{1-x}\text{W}_x\text{Se}_2$ monolayers also support such band bowing effect (Fig. 4(b)). Here, the

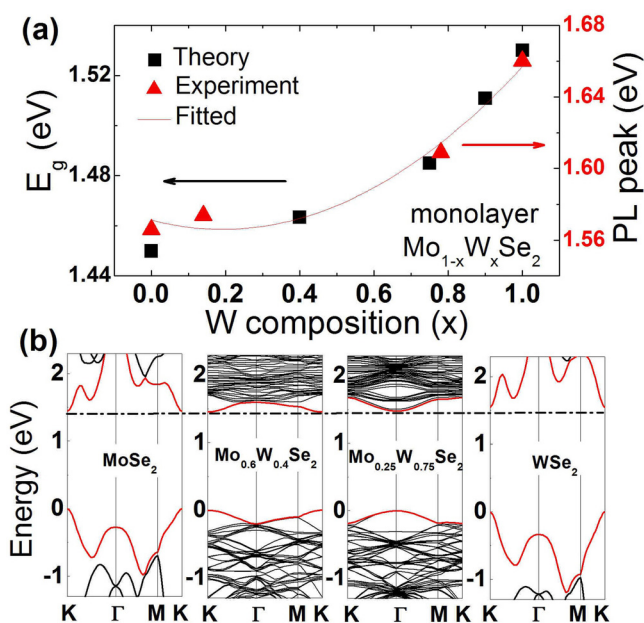


FIG. 4. (a) DFT-calculated direct bandgap and measured PL peak energy for monolayer $\text{Mo}_{1-x}\text{W}_x\text{Se}_2$ for different W compositions (x). Note that the DFT results are vertically offset to compensate the well-known DFT underestimation of E_g . (b) DFT-calculated band structure of $\text{Mo}_{1-x}\text{W}_x\text{Se}_2$ monolayers from $x=0$ to $x=1$. Since the supercell is large for the alloys, the bandgap convolutes to Γ or K symmetry points, whereas the direct gap is always at K point for MoSe_2 and WSe_2 .

DFT calculations were performed using VASP¹⁹ under the gradient approximation of Perdew-Burke-Ernzerhof.^{20,21} The band structures of the alloys were calculated using either 5×5 or 6×6 supercell. We randomly substituted Mo atoms by W atoms, and selected the structures whose correlation functions²² were close to that of a random alloy. In this way, the physical properties of the truly random alloy can be well simulated. The formation energy of the alloy was calculated to be -3 meV and -4 meV per cation for $x = 0.25$ and 0.6 , respectively. Therefore, phase separation is not energetically favorable, which agrees with the experimentally observed stability of 2D alloys. More importantly, the DFT calculations indeed show that small amount of Mo incorporation into WSe_2 rapidly reduces the bandgap toward that of MoSe_2 . Partial charge density wave calculations reveal that the CBM states of the alloys are strongly localized around

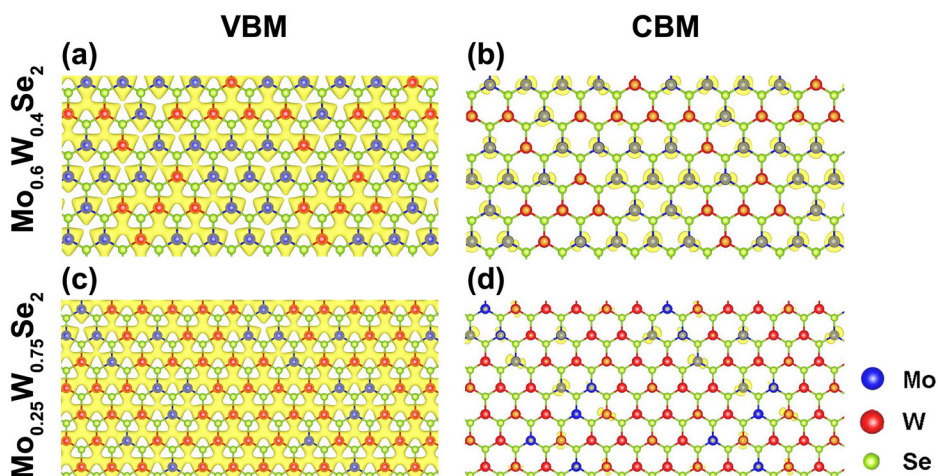


FIG. 5. (a) and (b) Charge density at the VBM and CBM states of $\text{Mo}_{0.6}\text{W}_{0.4}\text{Se}_2$. The isosurface corresponds to 15% of the maximum value. (c) and (d) Same for $\text{Mo}_{0.25}\text{W}_{0.75}\text{Se}_2$. The Charge density graph at the CBM clearly shows that the CBM states are strongly localized around Mo atoms due to the lower d_z orbital energies compared to that of WSe_2 .

the Mo atoms (Figs. 5(b) and 5(d)). Typically, the CBM states of TMDs are mainly contributed by the d_z^2 orbital of the cation (metal) atoms. Because the d_z^2 orbital extends along the out-of-plane, z direction, the coupling between different cations is weak. Since the d_z^2 orbital of Mo is lower in energy than W (by 0.47 eV), combined with the weak inter-cation coupling, the CBM of the alloy is localized around the Mo atoms even at very low Mo fractions. Therefore, even a small amount of Mo rapidly reduces the $\text{Mo}_{1-x}\text{W}_x\text{Se}_2$ bandgap toward that of MoSe_2 . On the other hand, the VBM states mainly originate from the d_{xy} and $d_{x^2-y^2}$ orbitals of the cations. These states are extended along the in-plane, x - y direction, and therefore these orbitals are strongly coupled to each other. Such coupling delocalizes the wavefunction and the VBM states are distributed almost uniformly over all cations, regardless of the constituent. As a result, the VBM energy varies linearly with the W composition whereas the CBM deviates from the linearity. Combining variation of VBM and CBM as a function of W composition, the bandgap of the $\text{Mo}_{1-x}\text{W}_x\text{Se}_2$ monolayers display a large band bowing as shown in Fig. 4(a).

In conclusion, we have experimentally and theoretically demonstrated 2D $\text{Mo}_{1-x}\text{W}_x\text{Se}_2$ alloys. These 2D alloys are stable in ambient conditions and remain direct bandgap semiconductors with high photoluminescence intensity. Alloying allowed us to tune the fundamental bandgap values with tungsten composition. The bandgap does not scale linearly with composition, showing a large bandgap bowing effect. Our DFT calculations suggest that the CBM states are strongly localized around the d_z^2 orbitals of the Mo atoms, whereas the VBM is more uniformly contributed by the d_{xy} and $d_{x^2-y^2}$ orbitals of both Mo and W atoms. As a result, a small amount of Mo incorporated into WSe_2 rapidly pushes downward the CBM of the alloys. 2D semiconductor alloys offer a unique platform for implementation of a wide variety of potential technologies by designing physical properties of 2D materials on-demand. For example, the demonstrated tunable range of bandgaps fits the solar spectrum, pointing out possible applications in solar energy related applications.

This work was supported by the National Science Foundation under Grant No. DMR-1306601. J.L. and the

computational effort gratefully acknowledge support from the Natural Science Foundation of China for Distinguished Young Scholar (Grant Nos. 60925016 and 91233120). The nano-Auger and XPS part was a user project at the Molecular Foundry, which was supported by the Office of Science, Office of Basic Energy Sciences, of the U.S. Department of Energy under Contract No. DE-AC02-05CH11231

- ¹Q. H. Wang, K. Kalantar-Zadeh, A. Kis, J. N. Coleman, and M. S. Strano, *Nat. Nanotechnol.* **7**, 699 (2012).
- ²K. Mak, C. Lee, J. Hone, J. Shan, and T. F. Heinz, *Phys. Rev. Lett.* **105**, 136805 (2010).
- ³A. Splendiani, L. Sun, Y. Zhang, T. Li, J. Kim, C. Y. Chim, G. Galli, and F. Wang, *Nano Lett.* **10**, 1271 (2010).
- ⁴K. F. Mak, H. Ke, C. Lee, G. H. Lee, J. Hone, T. F. Heinz, and J. Shan, *Nature Mater.* **12**, 207–211 (2013).
- ⁵J. S. Ross, S. Wu, H. Yu, N. J. Ghimire, A. M. Jones, G. Aivazian, J. Yan, D. G. Mandrus, D. Xiao, W. Yao, and X. Xu, *Nat. Commun.* **4**, 1474 (2013).
- ⁶S. Tongay, J. Zhou, C. Ataca, K. Lo, T. S. Matthews, J. Li, J. C. Grossman, and J. Wu, *Nano Lett.* **12**, 5576 (2012).
- ⁷S. Tongay, J. Zhou, C. Ataca, J. Liu, J. S. Kang, T. S. Matthews, L. You, J. Li, J. C. Grossman, and J. Wu, *Nano Lett.* **13**, 2831 (2013).
- ⁸H.-K. Komsa, S. Kurasch, O. Lehtinen, U. Kaiser, and A. V. Krasheninnikov, *Phys. Rev. B* **88**, 035301 (2013).
- ⁹S. Tongay, J. Suh, C. Ataca, W. Fan, A. Luce, J. S. Kang, J. Liu, C. Ko, R. Raghunathanan, J. Zhou *et al.*, *Sci. Rep.* **3**, 2657 (2013).
- ¹⁰H. J. Conley, B. Wang, J. I. Ziegler, R. F. Haglund, S. T. Pantelides, and K. I. Bolontin, *Nano Lett.* **13**(8), 3626–3630 (2013).
- ¹¹J. Kang, S. Tongay, J. Li, and J. Wu, *J. Appl. Phys.* **113**, 143703 (2013).
- ¹²H.-P. Komsa and A. V. Krasheninnikov, *J. Phys. Chem. Lett.* **3**, 3652 (2012).
- ¹³Y. Chen, C. Xi, D. O. Dumcenco, Z. Liu, K. Suenaga, D. Wang, Z. Shuai, Y. S. Huang, and L. Xie, *ACS Nano* **7**(5), 4610–4616 (2013).
- ¹⁴H. Sahin, S. Tongay, S. Horzum, W. Fan, J. Zhou, J. Li, J. Wu, and F. M. Peeters, *Phys. Rev. B* **87**, 165409 (2013).
- ¹⁵W. Zhao, Z. Ghorannevis, L. Chu, M. Toh, C. Kloc, P. H. Tan, and G. Eda, *ACS Nano* **7**, 791 (2013).
- ¹⁶S.-H. Wei, S. B. Zhang, and A. Zunger, *J. Appl. Phys.* **87**, 1304 (2000).
- ¹⁷C. Ataca, H. Sahin, and S. Ciraci, *J. Phys. Chem. C* **116**, 8983–8999 (2012).
- ¹⁸J. Kang, S. Tongay, J. Zhou, J. Li, and J. Wu, *Appl. Phys. Lett.* **102**, 012111 (2013).
- ¹⁹G. Kresse and J. Hafner, *Phys. Rev. B* **47**, 558 (1993).
- ²⁰G. Kresse and F. Furthmuller, *Phys. Rev. B* **54**, 11169 (1996).
- ²¹J. P. Perdew, K. Burke, and M. Ernzerhof, *Phys. Rev. Lett.* **77**, 3865 (1996).
- ²²A. Zunger, S.-H. Wei, L. G. Ferreira, and J. E. Bernard, *Phys. Rev. Lett.* **65**, 353 (1990).